Journal of
Synchrotron Radiation

ISSN 0909-0495

Received 18 September 2008
Accepted 11 March 2009

Analyses of the factors for the demagnetization of permanent magnets caused by high-energy electron irradiation

Yoshihiro Asano,[a]* Teruhiko Bizen[b] and Xavier Maréchal[b]

[a]XFEL/RIKEN, SPring-8, Sayo, Hyogo 679-5148, Japan, and [b]Japan Synchrotron Radiation Research Institute, SPring-8, Sayo, Hyogo 679-5198, Japan. E-mail: asano@spring8.or.jp

Demagnetization owing to high-energy electron irradiation has been analyzed for permanent magnets used in insertion devices of synchrotron radiation sources, using the Monte Carlo code *FLUKA*. The experimental data of a thermally treated $Nd_2Fe_{14}B$ permanent magnet with a copper or a tantalum block at electron energies ranging from 2 to 8 GeV were compared with the calculation data of the absorbed doses, photoneutron production distributions and star densities. The results indicate that low-energy photoneutrons and bremsstrahlung photons are not involved in the demagnetization process, and suggest that the star density owing to the photoneutrons is strongly correlated with the demagnetization process.

Keywords: demagnetization; electron; Monte Carlo code *FLUKA*; SPring-8; insertion device; radiation damage; photoneutron; bremsstrahlung; $Nd_2Fe_{14}B$ magnet.

1. Introduction

In order to obtain an extremely high brilliant light source, insertion devices such as wigglers and undulators are installed in the storage ring of third-generation synchrotron radiation facilities. An insertion device consists of permanent magnets of the same magnetic field strength set in periodical arrays. A few percent variation in the magnetic field of the insertion device cannot be tolerated. Besides, the enhanced high qualities of the permanent magnets, such as the same strength with the same period, are strongly required for X-ray free-electron laser facilities as well as for the electron beam. On the other hand, the phenomenon of the reduction of the magnetic field strength owing to the irradiation of high-energy electrons, demagnetization, is well known (Petra *et al.*, 2003; Colomp *et al.*, 1993), so that an estimation of the possible damage and countermeasures are a crucial concern.

Many demagnetization experiments have been performed so far by using high-energy electrons (Luna & Maruyama, 1989; Okuda *et al.*, 1994; Bizen *et al.*, 2001, 2003*a*; Qiu *et al.*, 2007, 2008), neutrons (see, for example, Alderman *et al.*, 2002; Kawakubo *et al.*, 2004) and other high-energy particles (see, for example, Cost *et al.*, 1988; Blackmore, 1985). However, the mechanisms of the demagnetization owing to high-energy particle irradiation still have not been discussed in detail. High-energy electrons produce electromagnetic showers and neutrons by photonuclear reactions with a thick target block, so that the behaviors of the electrons, photons and neutrons within the magnet are important for investigation of the demagnetization process.

The main causes of demagnetization of permanent magnets are thermal effects, displacements and transmutations of the nuclei. Two theories related to thermal effects are usually propounded up to now for demagnetization owing to high-energy irradiation. One is Kähkönen's thermal spike (see, for example, Seitz & Koehler, 1956; Chadderton, 1965) model (Kähkönen *et al.*, 1994), which is based on the Curie temperature of the magnet. The other is Makita's demagnetization model (Makita *et al.*, 2004), which is based on the starting temperature for thermal demagnetization, and depends on the permeance of the magnet; in this model, demagnetization occurs when the temperature rises above the starting point of thermal demagnetization, even though the rising temperature is below the Curie temperature. The thermal spike and the rising-temperature models are fundamentally connected to the density of the knock-on atoms and the absorbed doses within the magnet, respectively. Transmutations and metallurgical/crystallographic changes such as displacements have also been proposed (Alderman & Job, 2000; Qiu *et al.*, 2008) as the causes of demagnetization. However, much contrary evidence has been reported such as fully recovered re-magnetization (see, for example, Okuda *et al.*, 1994; Cost *et al.*, 1988) after demagnetization owing to irradiation. Moreover, no effect was shown with irradiation by thermal neutrons up to fluences of 3×10^{12} cm^{-2} even though the permeance was very low at 0.29 (Alderman *et al.*, 2002). Up to 43% demagnetization was observed with thermal neutron fluences up to 8.9×10^{13} cm^{-2} for magnets with a permeance of 0.62 (Klaffky *et al.*, 2006). The authors, even in that case, show that the recoiled nucleus resulting from

thermal neutron capture reactions with boron-10, which is the constituent atom of the magnet, has enough energy to generate a thermal spike. The most effective quantity for estimating the effect of high-energy electrons on a permanent magnet for demagnetization is still not clear.

For the purpose of clarifying an index for evaluating the demagnetization of an insertion device owing to irradiation, we have estimated the absorbed doses, collision densities, star densities and residual nuclei by using the Monte Carlo simulation code *FLUKA* (Fasso *et al.*, 2001). The results have been compared with experiments, which were performed using thermally treated permanent magnets to reduce demagnetization by thermal fluctuation, since these magnets are normally used for in-vacuum-type undulators (Bizen *et al.*, 2003*b*).

2. Experiments and calculation model

Experiments of demagnetization owing to high-energy electrons were performed by using the synchrotron booster of SPring-8 for energies of 4 to 8 GeV (Bizen *et al.*, 2007), while, for 2 GeV, experiments were carried out at the Pohang Accelerator Center (Bizen *et al.*, 2003a). All the magnets used in these experiments were thermally treated neodymium borate ($Nd_2Fe_{14}B$) magnets. These magnets, which are commonly used for in-vacuum-type undulators, are baked to stabilize their remanent magnetic field. Magnets of size 46 (width) × 12 (height) × 8 (thickness) mm were employed. A 100 (width) × 25 (height) × 40 (thickness) mm target block corresponding to the RF finger clamp used in in-vacuum-type undulators was installed directly in front of the magnets. The block was made either of copper for the 4 to 8 GeV experiments or of tantalum (Bizen, 2008) for the 8 GeV experiments. Note that for the 2 GeV experiments there was a gap between the magnet and the block. A water-cooling system kept the magnet temperature constant within 0.2 K. The block and the magnet were set into the beam dump of the SPring-8 booster synchrotron, which has a double cylindrical structure (the inner made of graphite and the outer made of iron). In the experiments performed with the copper block, we found that the rates of magnetic field loss were proportional to the number of irradiated electrons up to 1.4×10^{15} and that these rates depended on an exponential function of the electron energy (Bizen *et al.*, 2007). Therefore, the percentage of the magnetic field loss rate per one irradiated electron, $\Delta\varphi$, with the copper block could be expressed as follows,

$$\Delta\varphi(\%) = [-0.028 + 0.052\exp(-0.366E)] \times 10^{-13}N \quad (1)$$

for ($N \leq 1.4 \times 10^{15}$), where E is the electron energy in GeV and N is the number of irradiated electrons.

The experimental set-up at SPring-8 and the calculation configuration is illustrated in Fig. 1, along with the physical nomenclature of the magnet used in this paper. In the calculations for the SPring-8 experiments, we considered a graphite block as the core of the dump, set up just behind the magnet on the downstream side. During the SPring-8 experiments, the electron beam size was less than 2 mm horizontally and

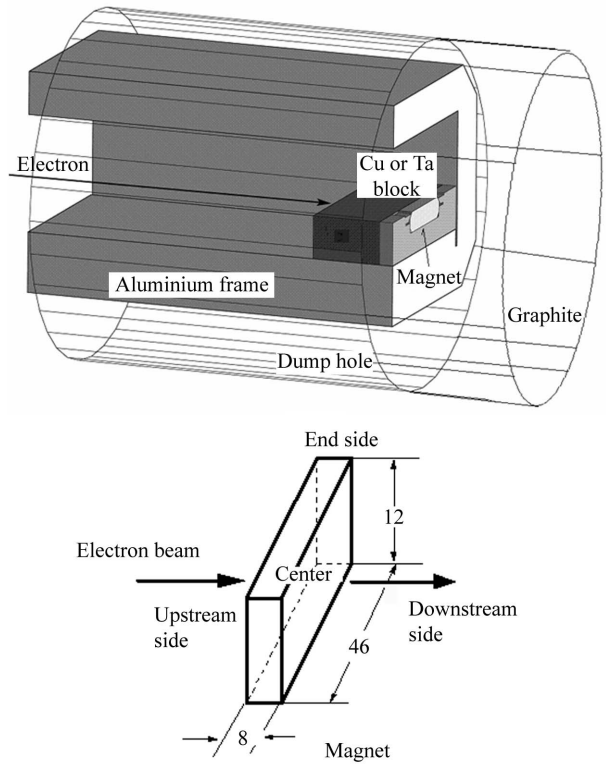

Figure 1
Illustration of the experimental set-up, and the $Nd_2Fe_{14}B$ permanent magnet nomenclature. The copper block was employed for experiments at all electron energies. The tantalum block was employed only for the 8 GeV experiment. For the 2 GeV experiment, there was a gap between the block and magnet, and no graphite. (Units: mm.)

0.2 mm vertically so that the spread of the beam size and the beam divergence were neglected in the simulations. The *FLUKA* calculations were performed for indirect (with a copper or a tantalum block on the upstream side of the magnet) and direct (without the block) irradiations. The calculation configurations are the same as those of the experiments.

As mentioned above, the absorbed dose, neutron collision density, star density distribution and residual nuclei were estimated to investigate the most effective quantities relevant to the demagnetization owing to high-energy electron irradiation, and compared with experiments. The absorbed dose within the magnet is directly related to heat production. Photoneutrons are produced by interactions between the bremsstrahlung of the electromagnetic showers owing to high-energy electrons and the materials through the process of photonuclear reactions such as giant-resonance, quasi-deuteron production and pion production processes. High-energy neutrons are well known to cause demagnetization, so the behavior of the photoneutrons is important. Stars, *i.e.* hadronic inelastic nuclear interactions accompanied by a transfer of energy from the incident particle to the nucleons of the block nucleus, can generate heated or evaporated particles and create thermal spikes. Some residual nuclei are also picked up such as ^{7}Li, ^{55}Fe, ^{54}Mn, ^{56}Mn, ^{53}Cr and ^{147}Nd, which are mainly produced by $^{10}B(n,\alpha)^{7}Li$, $^{56}Fe(\gamma,n)^{55}Fe$,

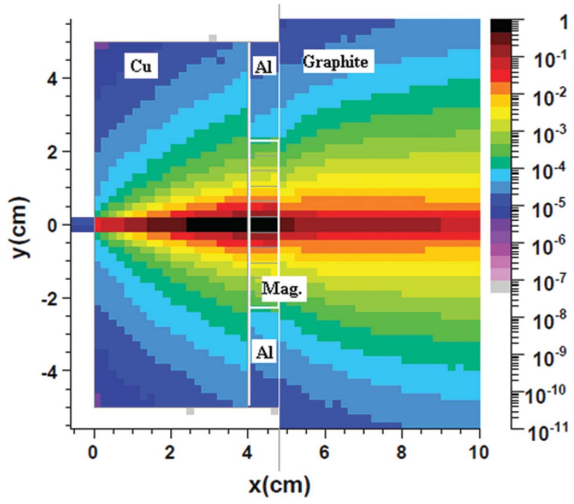

Figure 2
Absorbed dose distribution within the magnet owing to 8 GeV electrons with the copper block.

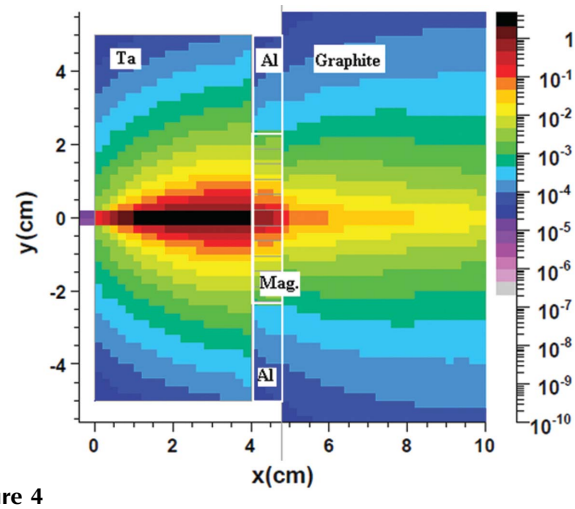

Figure 4
Absorbed dose distribution owing to 8 GeV electrons with the tantalum block.

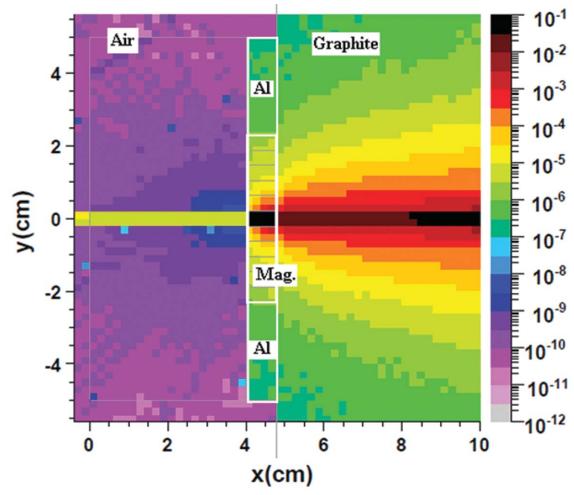

Figure 3
Absorbed dose distribution owing to 8 GeV electrons for direct irradiation (without block).

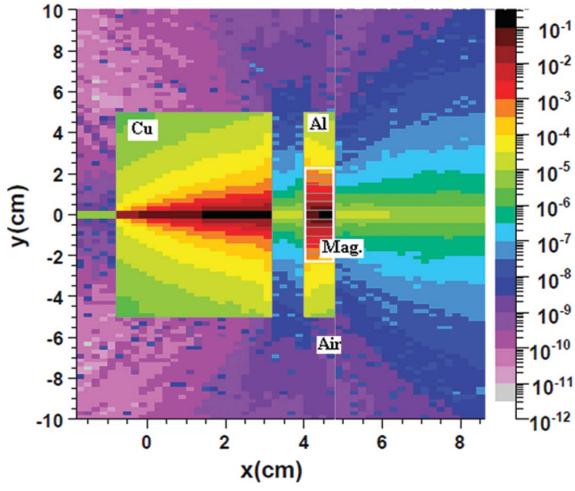

Figure 5
Absorbed dose distribution owing to 2 GeV electrons with the copper block. There was an air gap between the block and the magnet, and no graphite block in the experiments carried out at Pohang.

$^{54}Fe(n,\gamma)^{55}Fe$, $^{56}Fe(\gamma,n,p)^{54}Mn$, $^{54}Fe(n,p)^{54}Mn$, $^{56}Fe(n,p)^{56}Mn$, $^{56}Fe(n,\alpha)^{53}Cr$ and $^{148}Nd(\gamma,n)^{147}Nd$, $^{146}Nd(n,\gamma)^{147}Nd$ reactions, respectively. These residual nuclei are produced by the main nuclear reactions with the constituent atoms of the magnet.

3. Calculation results

3.1. Absorbed dose

The absorbed dose distributions are shown in Fig. 2 (with a copper block), Fig. 3 (without block) and Fig. 4 (with a tantalum block) in two-dimensional views. Fig. 5 shows the dose distribution owing to 2 GeV electrons with the copper block. From these calculations, it is clear that the differences between the absorbed dose distributions depend on the materials of the block and the electron energy. Figs. 6 and 7 show the absorbed dose distributions on the beam axis of the imparted electrons with the copper and tantalum blocks, respectively. The results without a block are also indicated. As shown in these figures, the dose within the magnet with the copper block is almost constant and about 1 Gy for 8 GeV electrons, and the dose with the tantalum block decreases quickly from 1 to 0.4 Gy. The absorbed dose within the magnet owing to 8 GeV electrons with the tantalum block on the upstream side is almost equal to that with the copper block. On the other hand, the dose owing to 8 GeV electrons with the tantalum block on the downstream side is almost equal to that owing to 2 GeV electrons with the copper block.

3.2. Neutron collision fluence

The neutron collision fluence within the magnet was calculated, and is shown in Figs. 8 and 9 for the center and end side of the magnet, respectively. In these calculations, 0.4032 cm^3 was employed for the detector volume (the magnet was separated into 11 segments in the direction parallel to the electron beam axis). As shown in these figures, the neutron

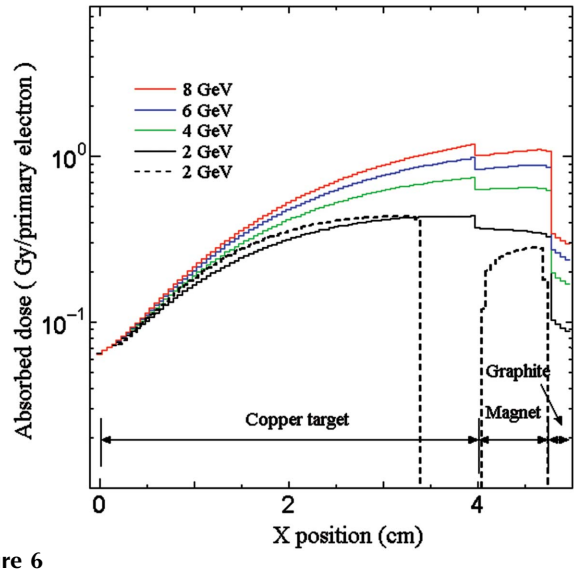

Figure 6
Absorbed dose distribution on the axis of the electron beam with the copper block. The dotted line indicates the dose owing to 2 GeV electrons for the experimental conditions at Pohang.

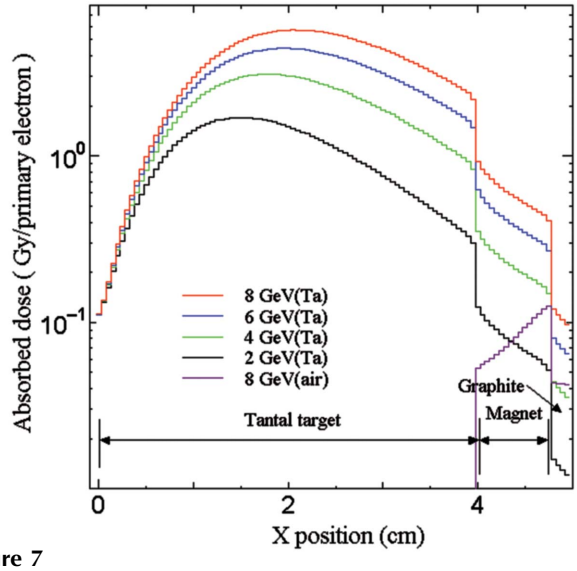

Figure 7
Absorbed dose distribution on the axis of the electron beam with the tantalum block and without a block.

collision fluence at the center of the magnet is higher with the tantalum block than with the copper block in the low energy region, below about 1 MeV. These relations are reversed in the high-energy region, above about 1 MeV. The difference between neutron collision fluences at the center of the magnet without a target calculated at 2 and 8 GeV are small in comparison with the cases with the copper block.

The neutron collision fluences owing to 8 GeV electrons within the end side part of the magnet, as shown in Fig. 9, are higher for the tantalum block than for the copper block below about 1 MeV, and almost the same above that energy. Without a block, the neutron collision fluences are much different at 2 and 8 GeV. The neutron collision fluence owing to 8 GeV electrons is almost negligible. At an energy of 1 MeV, the

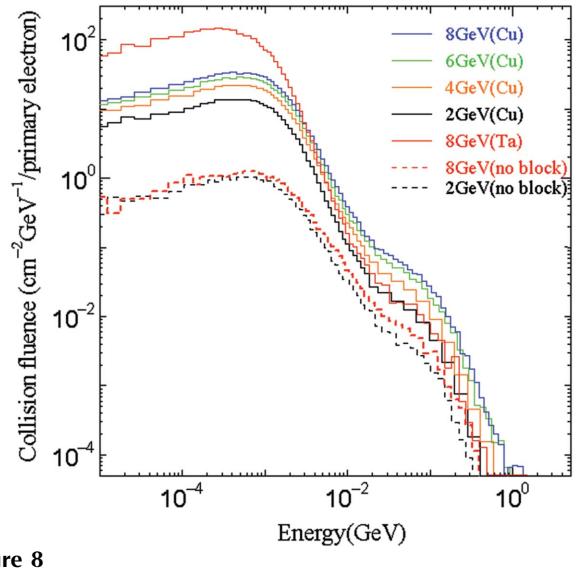

Figure 8
Neutron collision density distributions within the center of the magnet. The solid red line indicates the distribution owing to 8 GeV electrons with the tantalum block. Blue, green, orange and black solid lines are for 8 GeV, 6 GeV, 4 GeV and 2 GeV with the copper block, respectively. The red and black dotted lines are 8 GeV and 2 GeV without the block, respectively.

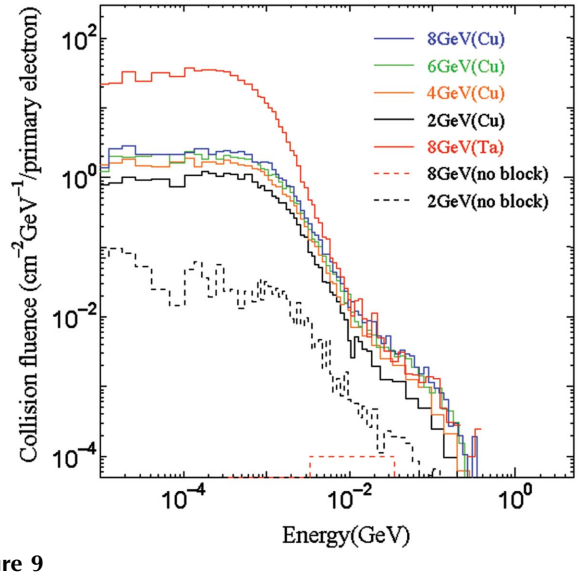

Figure 9
Neutron collision density distribution within the end of the magnet. Lines are the same as in Fig. 8.

neutron collision fluence within the center of the magnet owing to 2 GeV electrons is almost the same as that obtained within the end side of the magnet for 8 GeV electrons.

3.3. Star densities owing to neutrons and photons

Figs. 10 to 13 show the star density distributions including elastic scattering within the magnet as a function of the cut-off energy of the neutrons, and Fig. 14 shows the star density including elastic scattering owing to bremsstrahlung photons. The stars over the cut-off energy were scored. The volume of the detectors employed for the simulations was set at 0.2 × 0.2

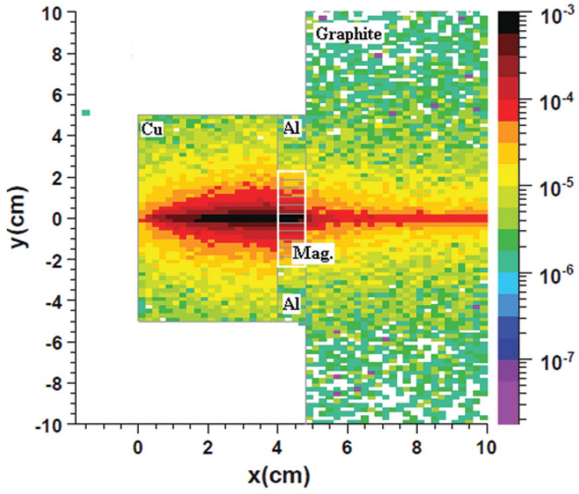

Figure 10
Star density distribution owing to 8 GeV electrons with the copper block and a cut-off energy of 20 MeV.

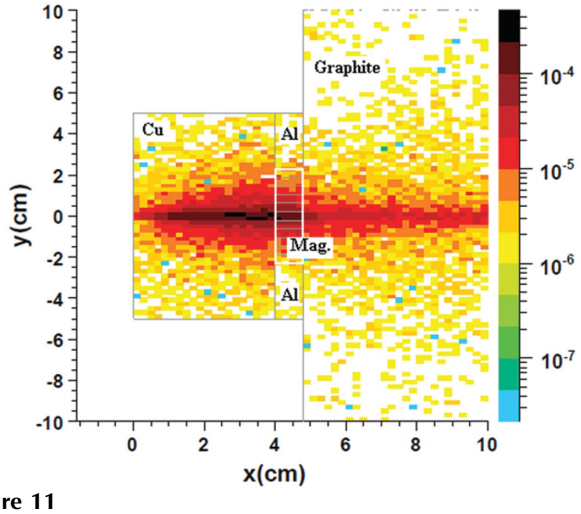

Figure 11
Star density distribution owing to photoneutrons for 8 GeV electrons with the copper block and a cut-off energy of 100 MeV.

× 0.8 cm. Figs. 10 and 11 are the star density distributions with the copper block, and Fig. 12 shows the distributions owing to 8 GeV electrons with the tantalum block. The star distributions with a cut-off energy of 100 MeV are quite different for the copper (Fig. 11) and tantalum (Fig. 12) blocks. Table 1 shows the star densities as a function of the cut-off energy for various electron energies. The star densities with the copper block are more than 2.5 times those obtained with the tantalum block. Figs. 13 and 14 show the star densities with cut-off energies of 500 MeV owing to photoneutrons and bremsstrahlung photons, respectively.

3.4. Residual nuclei

Table 2 shows the densities of the residual nuclei within the center of the magnet owing to high-energy electron irradiation as a function of the electron energy. In the table, the highest densities for ^{7}Li and ^{147}Nd are obtained in the case of the 8 GeV electron energy with the tantalum block. In the case of

Table 1
Calculation results of the average star density owing to photoneutrons at the beam center of the magnet as a function of the cut-off energy (cm^{-3} per primary electron).

Electron energy (GeV)	Block material	Cut-off energy (MeV) 20	100	500
8	Copper	5.4×10^{-4}	1.9×10^{-4}	1.0×10^{-5}
	Tantalum	1.6×10^{-4}	5.1×10^{-5}	2.1×10^{-6}
	Without block	8.4×10^{-5}	2.2×10^{-5}	3.4×10^{-8}
6	Copper	4.5×10^{-4}	1.3×10^{-4}	8.9×10^{-6}
4	Copper	3.4×10^{-4}	8.4×10^{-5}	4.4×10^{-6}
2†	Copper	1.2×10^{-4}	2.7×10^{-5}	1.6×10^{-6}

† A different geometry was employed in the case of 2 GeV.

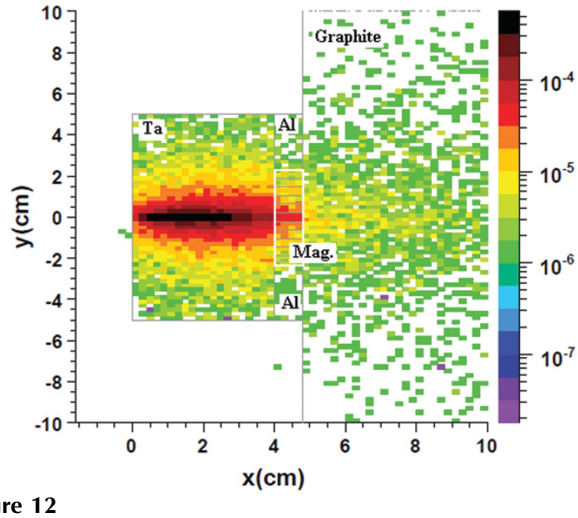

Figure 12
Star density distribution owing to photoneutrons for 8 GeV electrons with the tantalum block and a cut-off energy of 100 MeV.

the iron reactions (^{55}Fe, ^{54}Mn, ^{56}Mn and ^{53}Cr), the density of ^{55}Fe is highest for each electron energy. Besides, the highest density of the residual nuclei within the magnet is obtained at 8 GeV with the tantalum block for ^{55}Fe.

4. Discussions

As shown in Figs. 2 to 5, in all cases (with or without a block, at 2 to 8 GeV), almost all the energy owing to high-energy electrons is deposited at the center of the magnet. The star distributions are also the same as those of the energy deposition. These results are consistent with the results of the demagnetization experiments. The magnetic field losses occur mainly at the center of the magnet and the same distributions of the demagnetization were observed even for different electron energy (Bizen *et al.*, 2007). The absorbed doses on the electron beam axis within the center of the magnet as a function of the electron energy are shown in Fig. 15, including the results of the experiments. With the copper block, the doses within the magnet are almost the same at the upstream, center and downstream surface on the electron beam axis. On the other hand, the dose and the magnetic field loss increase with the electron energy at a different rate. The dose at the

Table 2
Calculation results of the density of the residual nuclei for each energy of electrons. Each nuclei, ^{7}Li, ^{55}Fe, ^{54}Mn, ^{56}Mn, ^{53}Cr and ^{147}Nd, are mainly produced by ^{10}B$(n,\alpha)^{7}$Li, ^{56}Fe$(\gamma,n)^{55}$Fe, ^{54}Fe$(n,\gamma)^{55}$Fe, ^{56}Fe$(\gamma,n,p)^{54}$Mn, ^{54}Fe$(n,p)^{54}$Mn, ^{56}Fe$(n,p)^{56}$Mn, ^{56}Fe$(n,\alpha)^{53}$Cr and ^{148}Nd$(\gamma,n)^{147}$Nd, ^{146}Nd$(n,\gamma)^{147}$Nd reactions, respectively.

Electron energy (GeV)	Block material	Residual nuclei (cm^{-3} per primary electron)					
		^{7}Li	^{55}Fe	^{54}Mn	^{56}Mn	^{53}Cr	^{147}Nd
2	Cu	1.8×10^{-5}	5.2×10^{-3}	3.3×10^{-4}	9.2×10^{-6}	2.3×10^{-5}	1.4×10^{-4}
4	Cu	3.5×10^{-5}	9.8×10^{-3}	6.4×10^{-4}	1.9×10^{-5}	4.3×10^{-5}	2.7×10^{-4}
6	Cu	4.6×10^{-5}	1.3×10^{-2}	8.4×10^{-4}	2.5×10^{-5}	5.8×10^{-5}	3.4×10^{-4}
8	Cu	5.5×10^{-5}	1.5×10^{-2}	1.0×10^{-3}	3.2×10^{-5}	7.1×10^{-5}	4.0×10^{-4}
8	Ta	8.5×10^{-5}	1.6×10^{-2}	6.9×10^{-4}	1.9×10^{-5}	2.6×10^{-5}	5.0×10^{-4}

upstream surface with the tantalum block is almost the same as that obtained with the copper block for 8 GeV electrons; however, the experimental results are different, about one-third of the magnetic field loss seen with the copper block. This suggests that the origins of the demagnetization are not limited to just the absorbed dose. This has been shown experimentally by several authors; for example, at the same dose the demagnetization is not the same for γ or electron irradiation (Okuda *et al.*, 1994).

For neutrons with an energy less than 1 MeV as shown in Figs. 8 and 9, the collision fluence at the end side of the magnet for 8 GeV electrons with the tantalum block is more than or almost equal to the collision fluence at the center of the magnet for 2 GeV electrons with the copper block. However, no demagnetization was detected at the end side of the magnet for the irradiation of 8 GeV electrons. This suggests that the low-energy neutrons produced by high-energy electrons up to 1.4×10^{15} irradiations do not cause the demagnetization, and this is consistent with experimental results (Alderman *et al.*, 2002) which do not show demagnetization under thermal neutron irradiation. For high-energy neutrons, the collision fluences at the center of the magnet are about one order higher or more than that at the end side of the magnet. This is consistent with experimental results (Kawakubo *et al.*, 2004) which have demonstrated that high-energy neutrons have a significant impact on the demagnetization.

In order to cause the demagnetization, the creation of a magnetic mutation region is necessary, and sufficient energy must be imparted through a process like knock-on atoms

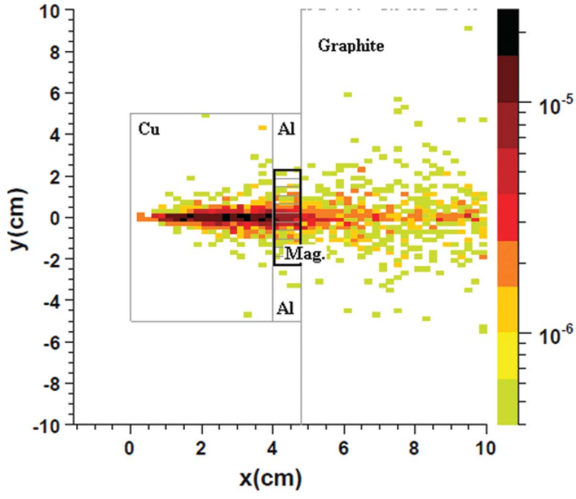

Figure 13
Star density distribution owing to photoneutrons for 8 GeV electrons with the copper block and a cut-off energy of 500 MeV.

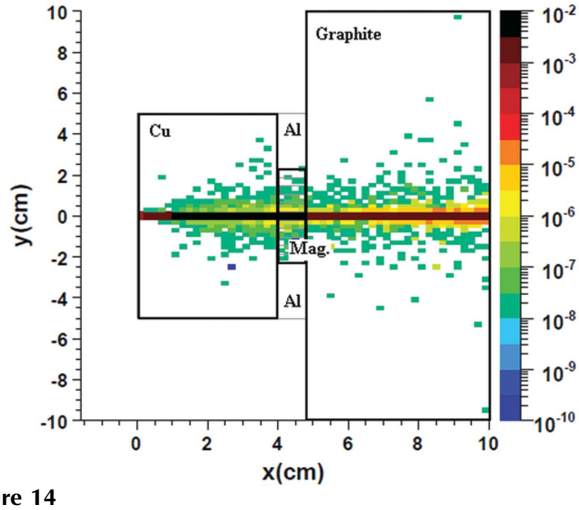

Figure 14
Star density distribution owing to bremsstrahlung photons for 8 GeV electrons with the tantalum block and a cut-off energy of 500 MeV.

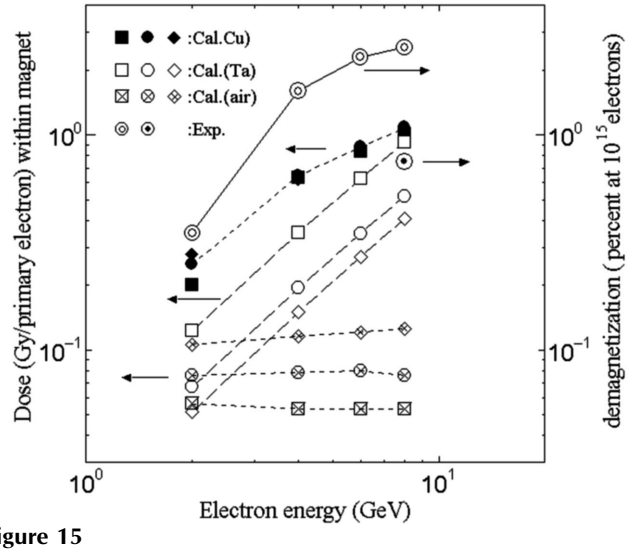

Figure 15
Absorbed dose around the electron beam axis and results of the demagnetization experiments. Full squares, full circles and full diamonds indicate the calculation results of the absorbed dose with the copper block at the upstream side, center and downstream side of the magnet, respectively. Open squares, open circles and open diamonds are the results obtained with the tantalum block. Squares with a cross, circles with a cross and diamonds with a cross are the results obtained without a block. Double circles are the experimental results with the copper block and the circles with a dot are the results obtained with the tantalum block (the values are given on the right-hand-side axis). The doses with the copper block owing to 2 GeV electrons indicate the calculation results for the configuration of the Pohang experiments.

(Kähkönen *et al.*, 1994; Makita *et al.*, 2004). A star is a hadronic inelastic interaction so that energy is imparted within a small region. Therefore the star density is a possible barometer of the demagnetization. The relations between the star densities owing to the photoneutrons and pions, and the experimental results of demagnetization are shown in Fig. 16 as a function of the incoming electron energy for the tantalum and copper blocks. The calculation results are normalized to the experimental results obtained with the 4 GeV electrons with the copper block. In the figure, we find that the star densities owing to the photoneutrons correlate strongly with the experimental results obtained with the copper block, and also the tantalum block. These are independent of the cut-off energy. However, in the case of bremsstrahlung photons, as shown in Fig. 17, the calculation results of the star densities with the tantalum block strongly depend on the cut-off energy, even though the electron energy dependence of the star densities in the copper block cases is consistent with the experiments. Fig. 18 shows the cut-off energy dependence of star densities owing to bremsstrahlung photons at 8 GeV with a tantalum block. These calculation data are normalized to the experimental data as in Figs. 16 and 17. These figures show that the star density owing to bremsstrahlung photons with an energy over ~40 MeV is consistent with experiments (Bizen *et al.*, 2007; Bizen, 2008) and experiments using γ-rays from cobalt-60 in which no demagnetization was observed (see, for example, Ikeda & Okuda, 1998).

Even though validity verifications of the nuclear reaction rates of the calculations are required, there are discrepancies between the experimental results and the calculations of the

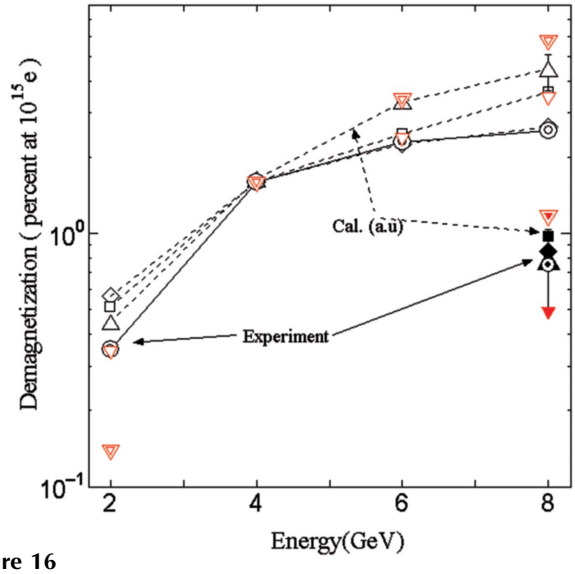

Figure 16
Relations between the results of the demagnetization experiments and the star densities owing to photoneutrons and pions as a function of the electron energy. The calculation results of the star densities are normalized to the 4 GeV experimental results. The double circles and circles with a dot are the experimental results with the copper and tantalum blocks, respectively. The open triangles, squares and diamonds are the calculation results of the star densities owing to the photoneutrons with the copper block for a cut-off energy of 500 MeV, 100 MeV and 20 MeV, respectively. The full triangle, square and diamond are the star densities owing to the photoneutrons with the tantalum block for a cut-off energy of 500 MeV, 100 MeV and 20 MeV, respectively. The red open inverse triangles and double inverse triangles are the star densities owing to the pions with the copper block for a cut-off energy of 100 MeV and 500 MeV, respectively. The red full inverse and double inverse triangles are the star densities owing to the pions with the tantalum block for a cut-off energy of 100 MeV and 500 MeV, respectively.

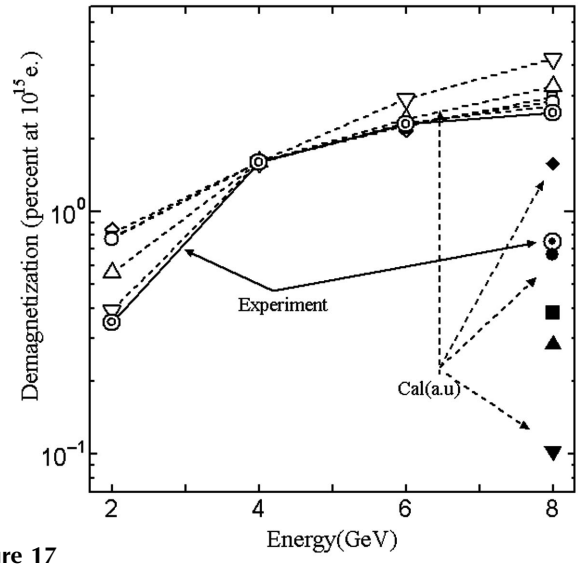

Figure 17
Relations between the results of the demagnetization experiments and the star densities owing to photons as a function of the electron energy. The calculation results of the star densities are normalized to the 4 GeV experimental results. The double circles and circle with a dot are the experimental results with the copper and the tantalum blocks, respectively. The open diamonds, circles, squares, triangles and inverted open triangles are the calculation results of the star densities with the copper block for a cut-off energy of 20 MeV, 40 MeV, 100 MeV, 500 MeV and 1 GeV, respectively. The full diamond, circle, square, triangle and inverted triangle are the star densities with the tantalum block for a cut-off energy of 20 MeV, 40 MeV, 100 MeV, 500 MeV and 1 GeV, respectively. The errors of these calculation results are less than 3%.

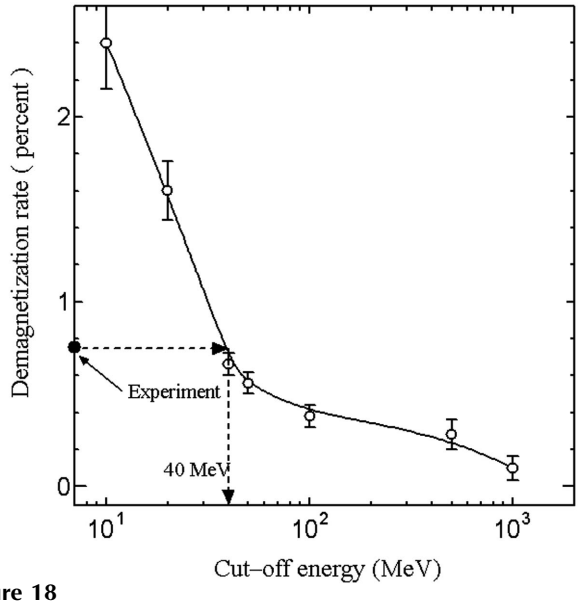

Figure 18
Calculation results of star densities owing to the bremsstrahlung photons for 8 GeV electrons as a function of the cut-off energy. The block is tantalum and the vertical axis is normalized as indicated in Fig. 17. The full circle is the experimental result with the tantalum block.

residual nuclei, as indicated in Table 2. Therefore nuclear transmutation is not the principal reason for the demagnetization. This is consistent with the fact that the magnet can fully recover the magnetic field after irradiation. At least, another process must be required such as energy impartment to generate the thermal spikes.

This suggests that the demagnetization of the thermal-treated neodymium borated magnet is caused by the stars owing to photoneutrons or owing to bremsstrahlung photons with energy over $\sim$40 MeV, but not by absorbed doses and nuclear transmutations.

5. Conclusions

The behavior of radiation within a magnet was analyzed by using *FLUKA*, and compared with experiments. We have confirmed that photoneutrons with energy less than 1 MeV do not cause the demagnetization. Inconsistencies with the experimental results attest that the absorbed dose within the magnet is not strongly connected to the demagnetization of the thermally treated neodymium borate permanent magnets. Nuclear transmutations also do not relate directly to the demagnetization. For high-energy electron irradiation, experimental results show that star density, which includes elastic and inelastic scattering owing to photoneutrons, is strongly correlated with the demagnetization process. If the stars owing to bremsstrahlung photons cause demagnetization, the energy of the photon needs to be greater than 40 MeV.

In the present analyses, some future problems are pointed out, one of which is to clarify the production process of the small magnetic mutation region from the mutation nuclei owing to the stars. Another is the relationship between the demagnetization and the absorbed dose. The absorbed dose and the star density are inextricably linked to each other. However, the contribution of the absorbed dose to the demagnetization process of the thermally treated $Nd_2Fe_{14}B$ magnets is still not clear.

References

Alderman, J. & Job, P. K. (2000). APS Report LS-290. Advanced Photon Source, Argonne National Laboratory, Argonne, IL, USA.

Alderman, J., Job, P. K., Martin, R. C., Simmons, C. M. & Owen, G. D. (2002). *Nucl. Instrum. Methods Phys. Res. A*, **481**, 9–28.

Bizen, T. (2008). *LCLS Undulator Magnet Irradiation Sensitivity Workshop*, SLAC, CA, USA.

Bizen, T., Asano, Y., Hara, T., Marechal, X. M., Seike, T., Tanaka, T., Kitamura, H., Lee, H. S., Kim, D. E. & Chung, C. W. (2003*b*). *AIP Conf. Proc.* **705**, 171–174.

Bizen, T., Asano, Y., Hara, T., Marechal, X. M., Seike, T., Tanaka, T., Lee, H. S., Kim, D. E., Chung, C. W. & Kitamura, H. (2003*a*). *Nucl. Instrum. Methods Phys. Res. A*, **515**, 850–852.

Bizen, T., Asano, Y., Marechal, X. M., Seike, T., Aoki, T., Fukami, K., Hosoda, N., Yonehara, H., Takagi, T., Hara, T., Tanaka, T. & Kitamura, H. (2007). *Nucl. Instrum. Methods Phys. Res. A*, **574**, 401–405.

Bizen, T., Tanaka, T., Asano, Y., Kim, D. E., Bak, J. S., Lee, H. S. & Kitamura, H. (2001). *Nucl. Instrum. Methods Phys. Res. A*, **467–468**, 185–189.

Blackmore, E. W. (1985). *IEEE Trans. Nucl. Sci.* **32**, 3669–3671.

Chadderton, L. T. (1965). *Radiation Damage in Crystals.* New York: Wiley.

Colomp, P., Oddolaye, T. & Elleaume, P. (1993). Technical Report ESRF/Mach-ID/93–09. ESRF, Grenoble, France.

Cost, J. R., Brown, R. D., Giorgi, A. L. & Stanley, J. T. (1988). *IEEE Trans. Magn.* **24**, 2016–2019.

Fasso, A., Ferrari, A., Ranft, J. & Sala, P. R. (2001). *Proceedings of the Monte Carlo 2000 Conference*, Lisbon, Portugal, pp. 955–960.

Ikeda, T. & Okuda, S. (1998). *Nucl. Instrum. Methods Phys. Res. A*, **407**, 439–442.

Kähkönen, O. P., Talvitie, M., Kautto, E. & Manninen, M. (1994). *Phys. Rev. B*, **49**, 6052–6057.

Kawakubo, T., Nakamura, E., Numajiri, M., Aoki, M., Hisamura, T. & Sugiyama, E. (2004). *Proceedings of the Ninth European Particle Accelerator Conference (EPAC 2004)*, Lucerne, Switzerland, pp. 1696–1698.

Klaffky, R., Lindstrom, R., Maranville, B., Shull, R., Micklich, B. J. & Vacca, J. (2006). *Proceedings of the Tenth European Particle Accelerator Conference (EPAC 2006)*, Edinburgh, Scotland, pp. 3589–3591.

Luna, H. B. & Maruyama, X. K. (1989). *Nucl. Instrum. Methods Phys. Res. A*, **285**, 349–354.

Makita, K., Kawakubo, T., Nakamura, E., Sugiyama, E. & Aoki, M. (2004). *J. Magn. Soc. Jpn*, **28**, 326–329.

Okuda, S., Ohashi, K. & Kobayashi, N. (1994). *Nucl. Instrum. Methods Phys. Res. B*, **94**, 227–230.

Petra, M., Hartog, P. K. D., Moog, E. R., Sasaki, S., Sereno, N. & Vasserman, I. B. (2003). *Nucl. Instrum. Methods Phys. Res. A*, **507**, 422–425.

Qiu, R., Lee, H. S., Hong, S., Li, J. & Bizen, T. (2007). *Nucl. Instrum. Methods Phys. Res. A*, **575**, 305–314.

Qiu, R., Lee, H. S., Li, J., Koo, T. Y. & Jang, T. H. (2008). *Nucl. Instrum. Methods Phys. Res. A*, **594**, 111–118.

Seitz, F. & Koehler, J. F. (1956). *Solid State Phys.* **2**, 305–448.